nature energy

Article

https://doi.org/10.1038/s41560-024-01465-2

Suppressing strain propagation in ultrahigh-Ni cathodes during fast charging via epitaxial entropy-assisted coating

Received: 22 May 2023

Accepted: 17 January 2024

Published online: 29 February 2024

Check for updates

Chen Zhao[1,9], Chuanwei Wang[2,9], Xiang Liu[1], Inhui Hwang[3], Tianyi Li[3], Xinwei Zhou[4], Jiecheng Diao[5,6], Junjing Deng[3], Yan Qin[1], Zhenzhen Yang[1], Guanyi Wang[4], Wenqian Xu[3], Chengjun Sun[3], Longlong Wu[7], Wonsuk Cha[3], Ian Robinson[5,7], Ross Harder[3], Yi Jiang[3], Tekin Bicer[3], Jun-Tao Li[2], Wenquan Lu[1], Luxi Li[3] ✉, Yuzi Liu[4] ✉, Shi-Gang Sun[8], Gui-Liang Xu[1] ✉ & Khalil Amine[1] ✉

Surface reconstruction and the associated severe strain propagation have long been reported as the major cause of cathode failure during fast charging and long-term cycling. Despite tremendous attempts, no known strategies can simultaneously address the electro-chemomechanical instability without sacrificing energy and power density. Here we report an epitaxial entropy-assisted coating strategy for ultrahigh-Ni $LiNi_xCo_yMn_{1-x-y}O_2$ ($x \geq 0.9$) cathodes via an oriented attachment-driven reaction between Wadsley–Roth phase-based oxides and the layered-oxide cathodes. The high anti-cracking and anti-corrosion tolerances as well as the fast ionic transport of the entropy-assisted surface effectively improved the fast charging/discharging capability, wide temperature tolerance and thermal stability of the ultrahigh-Ni cathodes. Comprehensive analysis from the primary and secondary particle level to the electrode level using multi-scale in situ synchrotron X-ray probes reveals greatly reduced lattice dislocations, anisotropic lattice strain and oxygen release as well as improved bulk/local structural stability, even when charging beyond the threshold state of charge (75%) of layered cathodes.

The high energy densities of Ni-rich layered oxides have made them promising cathodes for next-generation battery system to meet the ever-increasing energy demands of electric vehicles[1–3]. However, the intrinsic high reactivity of highly delithiated Ni-rich cathodes with electrolytes has led to a series of persistent structural fatigue issues including the layered-to-spinel/rock salt phase transformation[4] and lattice oxygen loss[5] at the surface or in near-surface structures, which deteriorate the cathode–electrolyte interphase (CEI) and increase the cell impedance. The reconstructed surface often further blocks the transport of lithium ions and electrons, leading to severe local charge heterogeneity from the particles across the entire electrodes[6,7]. Coupled with the inherent anisotropic lattice variation of layered

[1]Chemical Sciences and Engineering Division, Argonne National Laboratory, Lemont, IL, USA. [2]College of Energy, Xiamen University, Xiamen, China. [3]X-ray Science Division, Argonne National Laboratory, Lemont, IL, USA. [4]Center for Nanoscale Materials, Argonne National Laboratory, Lemont, IL, USA. [5]London Centre for Nanotechnology, University College London, London, UK. [6]Center for Transformative Science, ShanghaiTech University, Shanghai, China. [7]Condensed Matter Physics and Materials Science Department, Brookhaven National Laboratory, Upton, NY, USA. [8]Collaborative Innovation Center of Chemistry for Energy Materials, State Key Laboratory Physical Chemistry of Solid Surfaces, Department of Chemistry, Xiamen University, Xiamen, China. [9]These authors contributed equally: Chen Zhao, Chuanwei Wang. ✉e-mail: luxili@anl.gov; yuziliu@anl.gov; xug@anl.gov; amine@anl.gov

cathodes[8], a quick buildup of interfacial strain and stress is often observed, which tends to cause fatal mechanical breakdowns such as inter-granular[9] and intra-granular cracking[10]. Furthermore, these chain reactions will induce detrimental chemical crosstalk within the cells such as transition metal (TM) dissolution/migration[11] and gaseous generation/diffusion[12], notably deteriorating the graphite or lithium metal anode. These structural deformations will be dramatically aggravated when increasing the Ni content (Ni ≥ 0.9) or at high state of charge (SoC ≥ 80%) to extract higher energy densities[1]. These findings highlight the necessity of rational surface protection for ultrahigh-Ni cathodes towards harsh conditions such as fast charging[13–15], high voltage and extreme weather[16].

An ideal coating not only requires fast electron/ion transport to enable a fast charging capability but also is expected to have a high chemical tolerance of electrolytes and strong mechanical strength as well as robust adhesion with the bulk cathode phase to achieve long durability[17]. Unfortunately, the conventional coating strategies using metal oxides/fluorides[18], solid Li^+ conductors[19] and conductive polymers[20] via dry/wet mixing processing or physical/chemical vapour deposition still fall short of satisfying these criteria[21], owing to a lack of either the desired physiochemical functionalities or sufficient coating coverage and bonding strength (Supplementary Fig. 1), leading to a serious trade-off between capacity and stability.

High-entropy materials have been regarded as rising stars in renewable energy technology owing to their unpredicted physical, chemical and mechanical properties[22–25]. High-entropy oxide cathodes and high-entropy surface/bulk doping strategies have demonstrated improved structural stability in layered-oxide cathodes[26–29].

Inspired by the effect of entropy stabilization and given the oxide nature of $LiNi_xCo_yMn_{1-x-y}O_2$ (NCM) cathodes, in this Article we propose to develop an epitaxial entropy-assisted oxide coating via a surface fusion process to address the progressive surface-to-bulk structural fatigue of ultrahigh-Ni cathodes. Oriented attachment growth is the classical mode of crystallization by which atomic lattices of adjunct crystalline grains are aligned with good lattice matching to form larger crystals[30], which can be further extended in a chemical reaction-directed manner to synthesize new phases under high temperature or high pressure[31]. Our attention was drawn to Wadsley–Roth crystallographic shear structure-based oxides[32] (for example, $Nb_{12}WO_{33}$), which consist of a ReO_3-type block ($Im\bar{3}$) that is parallel to the $R\bar{3}m$ layered structure of NCM cathodes in the [100] direction (Fig. 1a and Supplementary Fig. 2). Such crystallographic structural similarities can hence initiate an oriented attachment-driven phase transformation under thermal equilibrium to form an epitaxial entropy-assisted oxide coating layer on the surface with good coating coverage, remarkably improving the robustness of the cathode surface. Moreover, Wadsley–Roth phases are a class of superionic conductors that can enable fast charging[32], overcoming the low ionic conductivity issue of conventional oxides[21]. The cooperative effect of epitaxial growth and an entropy-assisted surface paves the way for developing fatigue-free cathodes to achieve fast-charging and long-lasting rechargeable batteries.

Epitaxial entropy-assisted surface design

In this Article, a polycrystalline $LiNi_{0.9}Co_{0.05}Mn_{0.05}O_2$ (Ni90) cathode with an ultrahigh Ni content of 90 atomic percentage (at%) (Supplementary Fig. 3) is used as a representative material to show the advantages of epitaxial entropy-assisted surface design. Wadsley–Roth $Nb_{12}WO_{33}$ and ZrO_2 are exemplary coating precursors that facilitate the formation of the entropy-assisted coating layer when both are nanometres in size (Supplementary Fig. 4). We conducted in situ synchrotron high-energy X-ray diffraction (HEXRD) characterization to probe the dynamic phase evolution during high-temperature calcination of Ni90, $Nb_{12}WO_{33}$ and ZrO_2 (using an equal weight ratio to intensify the XRD signals). The results (Fig. 1b and Supplementary Fig. 5) show that all reactants could be well identified, and no obvious phase transformation was observed until the temperature reached 600 °C. Accompanied by the gradually decreased intensities of reactants, a series of new peaks emerged (Fig. 1b, dashed boxes), confirming the feasibility of forming new phases through the solid-state reaction of layered oxides and other lattice-matching oxides. To synthesize the epitaxial entropy-assisted surface-coated Ni90 cathode (denoted as EEC–Ni90), the weight ratio of Ni90, $Nb_{12}WO_{33}$ and ZrO_2 was optimized at 1:0.001:0.004 (see Methods for details). The morphological characterization of Ni90 and EEC–Ni90 cathode by scanning electron microscopy (SEM) shows no visible morphology changes after coating (Supplementary Fig. 3a–c and Supplementary Fig. 6a–c). The HEXRD patterns and Rietveld refinements of Ni90 (Supplementary Fig. 3d and Supplementary Table 1) and EEC–Ni90 (Supplementary Fig. 6d and Supplementary Table 2) showed that both samples exhibited the typical $R\bar{3}m$ structure with slight Li/Ni mixing, while no peaks belonging to the entropy-assisted oxide phase could be identified owing to its low weight fraction. High-resolution transmission electron microscopy (HRTEM) was thus used to probe the microstructures of the entropy-assisted coating layer of EEC–Ni90. As shown in Fig. 1c and Supplementary Fig. 7, instead of the original ZrO_2 or $Nb_{12}WO_{33}$ nanoparticles, a conformal layer with a thickness of ~20 nm was observed on the surface of multiple EEC–Ni90 particles. The corresponding energy dispersive spectroscopy (EDS) elemental mapping confirmed the entropy-assisted nature of the epitaxial coating layer as verified by the co-existence and homogeneous distribution of Ni, Co, Mn, Nb and Zr within the epitaxial coating layer. Note that W is difficult to detect by TEM owing to its extremely low weight ratio (0.1‰). The results indicate that small fractions of Ni, Co and Mn in NCM diffused from the surface and reacted with oxide coating precursors (ZrO_2 and $Nb_{12}WO_{33}$) during high-temperature calcination, resulting in the formation of the epitaxial coating layer. The co-existence of multiple elements in the coating layer will increase the resulted entropy. However, owing to the de-localization/broadening problems[33,34] of EDS analysis that will induce signals from nearby regions (bulk NCM in this case), the transition metal signals from NCM, in particular the dominant Ni (90 at.%), make it difficult to accurately quantify the composition and entropy of the epitaxial coating layer. Nevertheless, the HRTEM image and the selected area electron diffraction (SAED) of EEC–Ni90 (Fig. 1d) indicated that the EEC layer exhibited a layered-like structure, whose crystalline lattice was well aligned with the layered direction of the bulk cathode phase. Such an oriented EEC layer can achieve excellent lattice interlock, realizing robust adhesion and fast Li^+ transport during extended periods of cycling. Therefore, such oriented attachment-driven induced entropy-assisted coating formation is different from physical mixture of Ni-rich cathodes and high-entropy oxides[35].

Battery performance and post mortem analysis

The electrochemical performance of bare Ni90 and EEC–Ni90 cathodes was evaluated using lithium as reference and counter electrodes. An additional 2 wt% of vinylene carbonate (VC) additive was added into the GEN II (1.2 M $LiPF_6$ in ethylene carbonate/ethyl methyl carbonate, v/v 3/7) electrolyte to stabilize the anode and minimize Li metal interference during cathode performance evaluations (Supplementary Fig. 8).

The comparison of their initial differential capacity curves and voltage profiles (Supplementary Fig. 9) showed that the initial coulombic efficiency was increased from 86.28% to 92.35%, indicating the effectiveness of the EEC layer in enhancing (de)lithiation reversibility. Moreover, the detrimental H^2–H^3 phase transition was effectively postponed from 0.7 SoC to 0.75 SoC after coating, and more Li^+ had been extracted upon charging to the same cut-off voltage of 4.3 V, indicating facilitated Li^+ diffusion and boosted redox kinetics by the EEC layer. Galvanostatic intermittent titration technique (GITT) test results (Supplementary Fig. 10) illustrated that EEC–Ni90 exhibited smaller voltage polarization than bare Ni90, and the Li^+ diffusion coefficient

https://doi.org/10.1038/s41560-024-01465-2

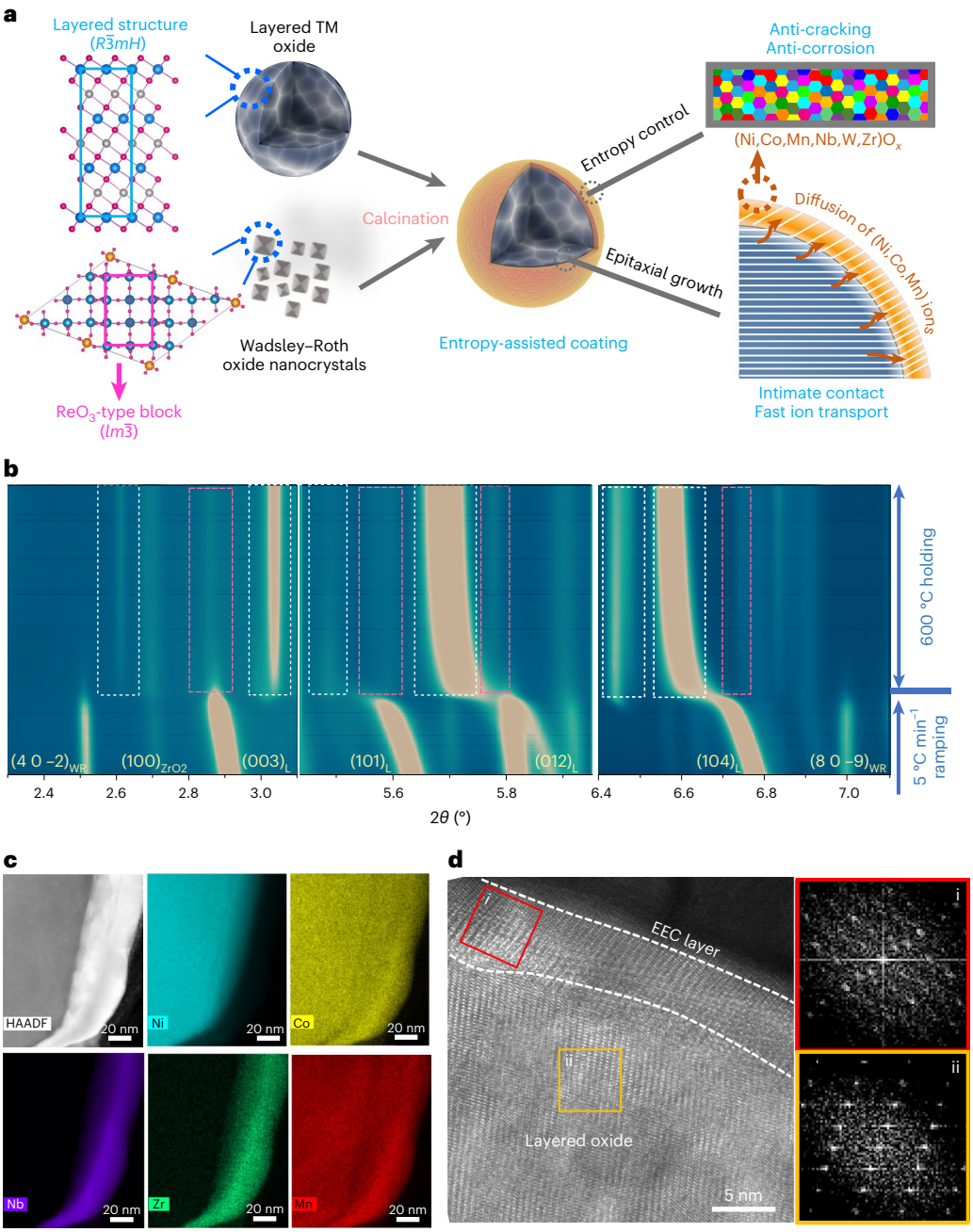

Fig. 1 | The design principle and structures of epitaxial entropy-assisted coating. a, Schematic illustrations of the entropy-assisted surface design for ultrahigh-Ni cathodes. The oriented attachment-driven phase transformation under thermal equilibrium of Wadsley–Roth nanocrystals and layered structure can induce epitaxial entropy-assisted coating layer formation on the NCM surface, achieving good cathode anti-corrosion and anti-cracking tolerances with fast ion transportation. **b**, In situ HEXRD during heating of Ni90 (L), nano-$Nb_{12}WO_{33}$ (WR) and nano-ZrO_2 (ZrO2) with equal weight ratio. Pink dashed boxes indicate pristine layer phase. White dashed boxes indicate emerging new peaks. **c**, HAADF–TEM and corresponding EDS element mappings of EEC–Ni90. **d**, High-resolution TEM image and fast Fourier transform patterns of selected region i (red) and ii (orange). The layer outside the EEC layer is Au for the purpose of protecting samples during focused ion beam TEM sample preparation.

at the same SoC was doubled in EEC–Ni90, confirming the facilitated Li^+ transport owing to the EEC layer.

As shown in Fig. 2a, EEC–Ni90 demonstrated a much higher specific capacity (186.5 mAh g^{-1}) and retention rate (95.98%) than Ni90 (137.7 mAh g^{-1} and 78.91%) after 200 cycles at 1.0C (1C, 220 mA g^{-1}). In addition, the blocked Li^+ diffusion at the reconstructed surface together with severe transition metal migration and oxygen loss[36] led to sharp voltage polarization during cycling of the bare Ni90 cathode (Fig. 2b). By sharp contrast, EEC–Ni90 could maintain a stable voltage profile even when charged to a higher SoC (Fig. 2b). Moreover, the SoC heterogeneity can often cause particle cracking and subsequent electrolyte penetration/corrosion, which has been considered as the main origin of the accelerated degradation of the H^2–H^3 phase transition and capacity fading of Ni-rich cathodes[37]. As shown in Supplementary Fig. 11, Ni90 suffered from obvious peak shifts and H^2–H^3 fading whereas EEC–Ni90 still exhibited stable phase transition behaviour during repeated charge/discharge, confirming the effectiveness of the EEC layer in mitigating the surface-initiated structure degradation over cycling.

https://doi.org/10.1038/s41560-024-01465-2

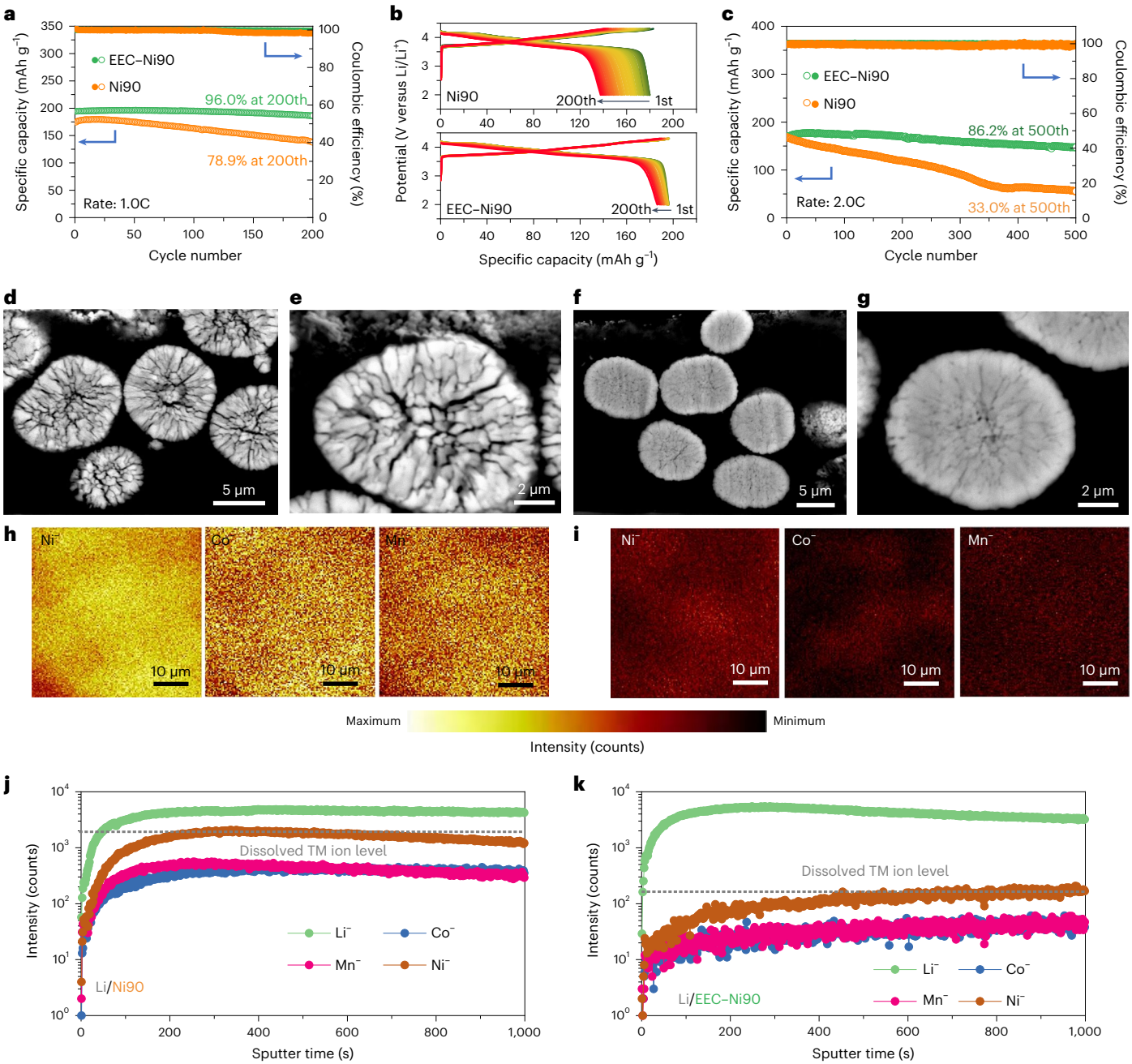

Fig. 2 | Electrochemical and post mortem evaluations. a, Cycling performance of bare Ni90 and EEC–Ni90 cathode at 1.0C. **b**, The corresponding voltage profiles of bare Ni90 and EEC–Ni90 cathode at 1.0C. **c**, Cycling performance of the bare Ni90 and EEC–Ni90 cathode at 2.0C. Hollow and solid symbols in **a** and **c** represent discharge specific capacity and Coulombic efficiency, respectively. **d**–**g**, Low- (**d**,**f**) and high- (**e**,**g**) magnification cross-section SEM images of cycled Ni90 (**d**,**e**) and EEC–Ni90 (**f**,**g**) cathodes after 500 cycles at 2.0C. **h**–**k**, ToF–SIMS secondary elements mapping (**h**,**i**) and depth profiles (**j**,**k**) of cycled Li metal anode after 500 cycles at 2C when coupling with Ni90 (**h**,**j**) and EEC–Ni90 (**i**,**k**) cathodes.

At a higher rate of 2C (Fig. 2c), EEC–Ni90 cathode could still deliver a high initial capacity of 171.1 mAh g^{-1} with a good retention of ~86% after 500 cycles at 2C, while bare Ni90 cathode exhibits a continuous capacity fading with a retention rate of only 33% after 500 cycles. A comprehensive comparison with literature shows that EEC–Ni90 outperforms numerous reported ultrahigh-Ni polycrystalline cathodes in terms of C rate, cycle number and cycle stability (Supplementary Fig. 12 and Table 3), consolidating the advantages of epitaxial entropy-assisted coating over existing strategies.

Moreover, post mortem characterization of the corresponding cycled electrodes reveals the greatly enhanced electrochemomechanical stability of the ultrahigh-Ni cathode owing to the EEC layer during fast charging and long-term cycling. Obvious and widespread inter-granular and intra-granular cracks were identified in the case of cycled bare Ni90 particles (Fig. 2d,e). These cracks will accelerate the parasitic reactions of Ni90 particles with the electrolytes and promote the dissolution/migration of transition metals and the formation of thick CEI, leading to rapid degradation of the ultrahigh-Ni cathode. By sharp contrast, cycled EEC–Ni90 particles did not show obvious cracks formation thanks to the protection of the epitaxial entropy-assisted coating layer (Fig. 2f,g). Moreover, a robust CEI layer with higher contents of O–C=O and LiF species was formed in the case

https://doi.org/10.1038/s41560-024-01465-2

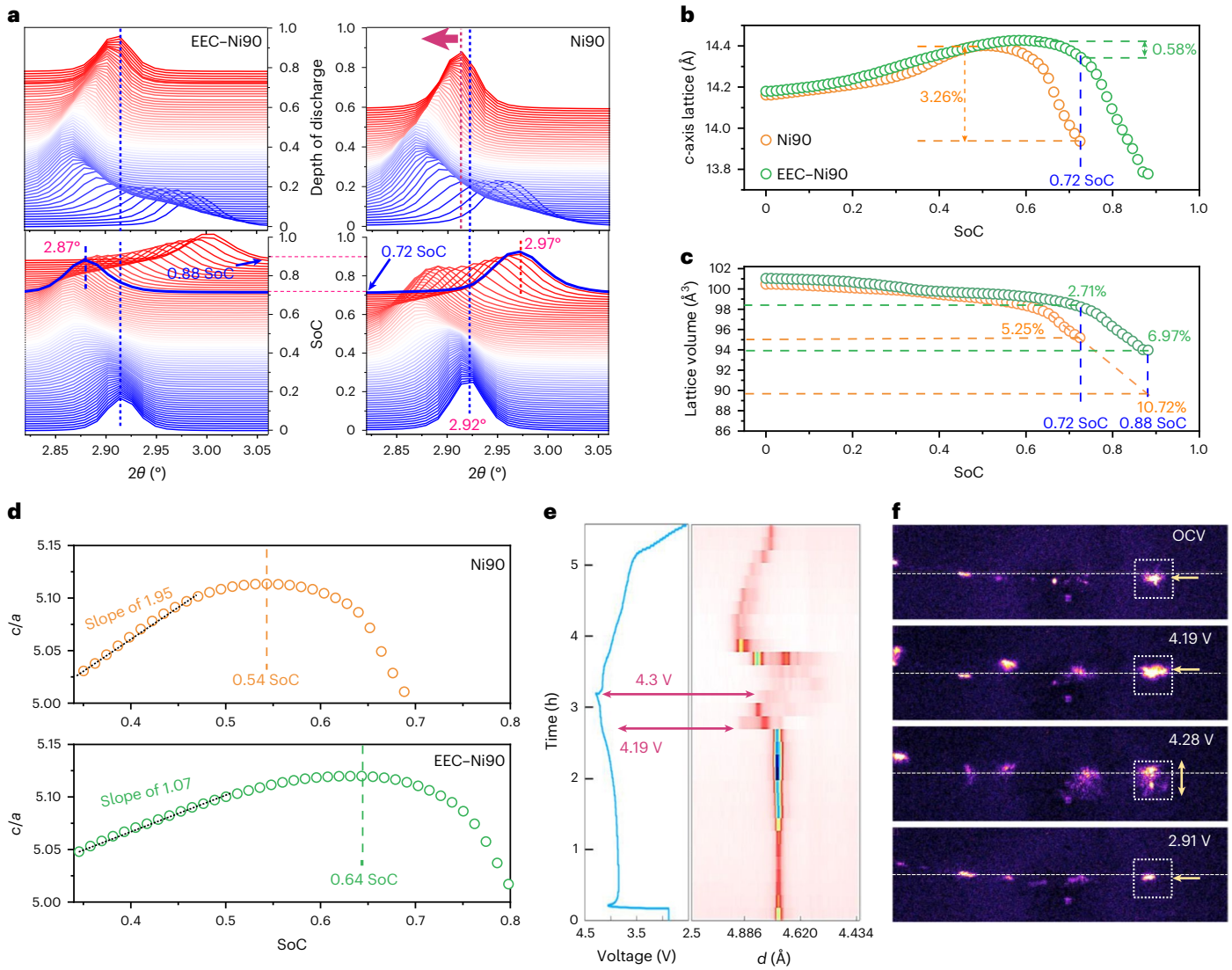

Fig. 3 | Bulk and local phase structure stability characterizations. a–d, In situ HEXRD patterns of (003) peaks (**a**), *c*-lattice parameter (**b**), lattice volume (**c**) and *c*/*a* (**d**) changes of EEC–Ni90 and Ni90 cathodes during charge/discharge. **e**,**f**, In situ CMCD characterization of EEC–Ni90 cathode during charge/discharge: the voltage profiles (left) and azimuthal average (right) of (003) peak during the initial charge/discharge of EEC–Ni90 cathode at 0.3C (**e**) and selected CMCD patterns for the Debye–Scherrer ring of the (003) peak at open-circuit voltage (OCV), 4.19 V (charge), 4.28 V (charge) and 2.91 V (discharge) (**f**). The arrows indicate the (003) reflection positions of selected bright diffraction spots. *d*, *d* spacing of (003) peak. The direct beam is on the top side of the diffraction patterns.

of cycled EEC–Ni90, indicating that entropy regulation could also stabilize the interfacial properties of the Ni-rich cathode (Supplementary Fig. 13). These results were further supported by the time-of-flight secondary ion mass spectrometry (ToF–SIMS) characterization of cycled Li metal in the Li/Ni90 and Li/EEC–Ni90 cells after 500 cycles at 2C. As shown in Fig. 2h,j, severe crossover of Ni^-, Co^- and Mn^- was found in the case of cycled bare Ni90 cell, confirming strong transition metal dissolution and crossover contamination after extended cycling. This process not only results in severe cathode surface reconstruction but also dramatically alters the anode solid electrolyte interphase composition and structure[11], leading to accelerated cell degradation. By sharp contrast, no obvious signals of Ni^-/Co^-/Mn^- can be observed in the case of the cycled EEC–Ni90 cell, indicating notably suppressed chemical crosstalk (Fig. 2i,k).

Even without VC additive in the electrolyte, EEC–Ni90 cathode still shows great improvement over bare Ni90 cathode, such as cycling stability (Supplementary Fig. 14), rate performance and fast charging (5C) performance (Supplementary Fig. 15) and high/low-temperature tolerance (Supplementary Figs. 16 and 17). Furthermore, a Li/EEC–Ni90 pouch cell (5 cm × 8 cm) could deliver a high specific capacity of >210 mAh g^{-1} with stable output voltage and structural reversibility during cycling (Supplementary Fig. 18).

In situ characterization

In situ HEXRD was performed to track the phase transformation of the bare Ni90 and EEC–Ni90 cathodes during charge/discharge. Overall, both cathodes exhibited typical H^1–M–H^2–H^3 phase transition features (Supplementary Fig. 19a,b)[38]. It was noted that the SoC is more accurate than the charge cut-off voltage in comparing the structural stability of Ni-rich cathodes[8], which represents the actual amount of extracted Li^+ from NCM cathodes. As shown in Fig. 3a, Ni90 can only deliver a maximum SoC of 0.72 together with a severe lattice contraction due to decreased O–O coulombic repulsion, as evidenced by a dramatic shift of the (003) peak from 2.92° to 2.97°. As a comparison, at the same SoC of 0.72, EEC–Ni90 was still at the stage of smooth lattice expansion, indicating stronger oxygen stability and hence achieving a higher

https://doi.org/10.1038/s41560-024-01465-2

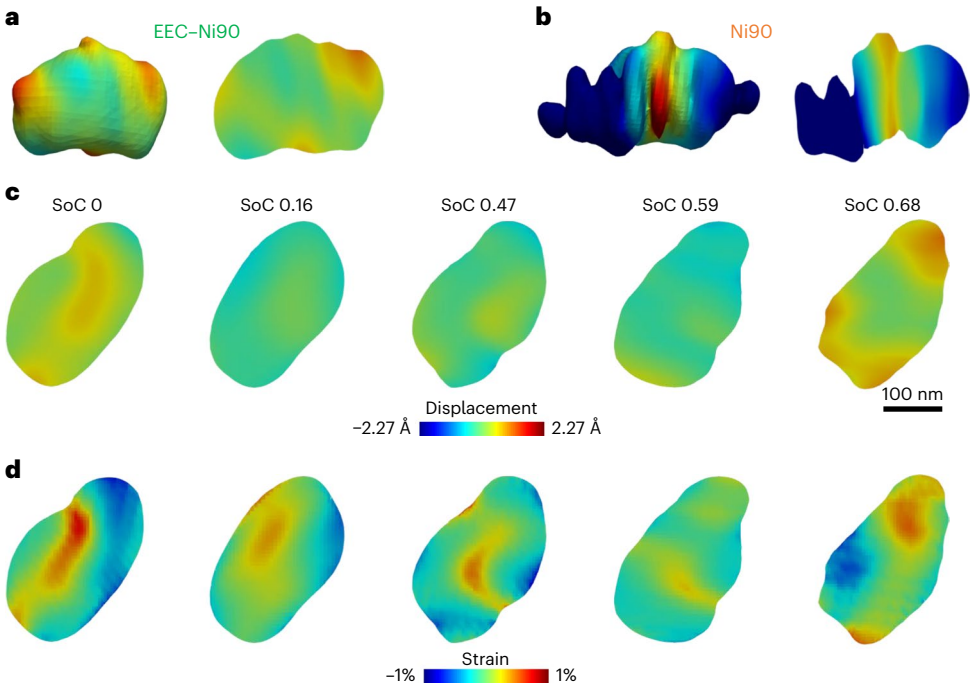

Fig. 4 | Strain evaluation within the cathode particle through BCDI characterizations. a,**b**, Three-dimensional isosurface rendering and cross-section atomic displacement field images of EEC–Ni90 (**a**) and Ni90 (**b**) cathodes after exposure to electrolytes for 30 h. **c**,**d**, In situ BCDI images of EEC–Ni90 cathode in the atomic displacement (**c**) and strain (**d**) field at different SoC.

maximum SoC of 0.88 when charged to the same cut-off voltage of 4.3 V (Fig. 3a). Nevertheless, despite a higher SoC, EEC–Ni90 exhibited improved structural reversibility compared with Ni90, as evidenced by the larger peak deviation in the bare Ni90 cathode after discharge while the (003) peak of the EEC–Ni90 cathode could almost return to its original position (Fig. 3a and Supplementary Fig. 19c).

Rietveld refinements on all the in situ HEXRD patterns were further processed to obtain the evolution of the lattice parameters during charging (Fig. 3b,c and Supplementary Fig. 20). As shown, Ni90 exhibited an abrupt *c* lattice parameter contraction of 3.26% and volume shrinkage of 5.25% (Fig. 3b,c). By sharp contrast, at the same SoC of 0.72, EEC–Ni90 exhibited much gentler variations in both lattice parameters (0.58% and 2.71%, respectively), indicating effective mitigation of lattice displacements and an anisotropic volume change (~50%) by the EEC layer coating. Such a difference will be exacerbated if Ni90 is charged to the same SoC (0.88) as EEC–Ni90 (Fig. 3c), indicating its poor structural stability at high voltage. Furthermore, an obvious slowdown of c/a shear strain buildup[39] by ~50% was observed in the case of EEC–Ni90 (Fig. 3d), confirming that the EEC layer could suppress the accumulation of lattice strain inside the particles to enhance the structural stability.

In situ coherent multi-crystal diffraction (CMCD) was also conducted to investigate the local phase structure transformation of EEC–Ni90, as the submicrometer-sized coherent X-ray beam could simultaneously probe dozens of crystals as well as provide the individual behaviour from one single crystal[40]. The diffraction patterns and the azimuthal average of the (003) peaks are shown in Fig. 3e,f, while the selected bright diffraction spots (square box) were used to track individual crystal behaviour. During charging at an elevated rate of 0.3C, no obvious pattern drifting could be observed before charging to 4.19 V, which was consistent with the bulk in situ HEXRD result. The slight shifting to a lower angle or larger *d* spacing corresponded to the *c*-axis expansion because of the coulombic repulsion between oxygen planes of Ni-rich cathodes. Further charging to 4.3 V resulted in the diffusion and span of the patterns to a higher angle or smaller *d* spacing, corresponding to the lattice contraction. Nevertheless, on discharging back to 2.91 V, both diffraction patterns and bright diffraction spots could return to their original positions, indicating a highly reversible phase transition process (Supplementary Video 1).

The Bragg coherent diffractive imaging (BCDI) technique[41–43] was used to directly visualize the nucleation of lattice dislocations and microstrain as well as their dynamics in EEC–Ni90 and Ni90 cathodes. Figure 4a,b shows the three-dimensional (3D) isosurface rendering images and the displacement slices taken from the centre of the crystals imaged with the (003) reflection. Red and blue colours represent the displacements from the ideal crystal lattice along or opposite to the (003) direction, respectively. As shown, the tolerance against commercial liquid electrolytes was greatly improved by EEC coating. After immersion into the electrolytes for 30 h, EEC–Ni90 still showed smooth particle morphology and only slight atomic displacement on the surface, whereas Ni90 without surface protection exhibited severe atomic displacement throughout the whole particle owing to electrolyte corrosion.

In situ BCDI was further conducted on the EEC–Ni90 cathode during charge at 0.1C (Supplementary Fig. 21). The atomic displacement field and the strain field images at different SoC are shown in Fig. 4c,d. Before the charge, we observed the co-existence of compressive (red colour) and tensile (blue colour) strain in the EEC–Ni90 particle, which has been observed in other pristine layered-oxide cathodes and has been attributed to the native structural defects (for example, heterogeneous Li distribution) during the manufacturing process[43,44]. Upon charging to an SoC of ~60%, the initial strain gradually disappeared owing to the rearrangements of Li occupancies in Li layers driven by delithiation, while no other displacements or strain generation were visible, indicating good structural stability. At an SoC of ~70%, slight tensile and compressive strain started to appear on the particle surface, which is reasonable owing to the faster Li^+ extraction at the surface. Overall, during the entire charging process with a high SoC up to ~70%, the EEC–Ni90 particle did not exhibit obvious morphology changes and singularity characteristic of dislocations, which is in contrast to

https://doi.org/10.1038/s41560-024-01465-2

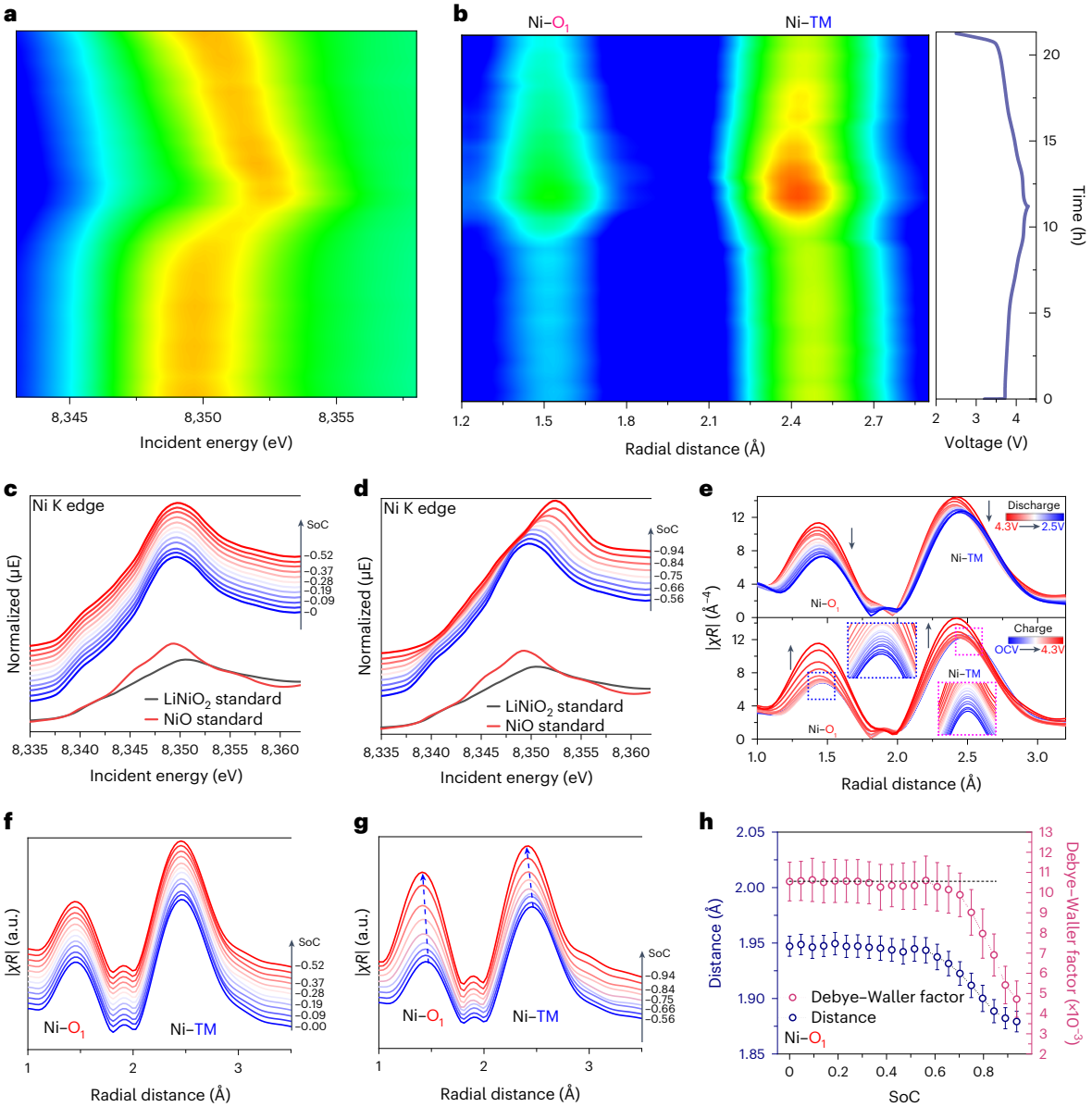

Fig. 5 | Local structure/environment analysis during operation. a,**b**, In situ XANES contour (**a**) and in situ EXAFS contour (**b**) combined with the voltage profiles of EEC–Ni90 during the initial cycle. **c**,**d**, In situ XANES spectra combined with standard $LiNiO_2$ (Ni^{III}) and NiO (Ni^{II}) samples of EEC–Ni90 during initial charging process when 0 < SoC < 0.52 (**c**) and 0.56 < SoC < 0.94 (**d**). **e**, In situ EXAFS spectra of EEC–Ni90 during the initial cycle. **f**,**g**, In situ EXAFS fitting results of EEC–Ni90 during the initial cycle when 0 < SoC < 0.52 (**f**) and 0.56 < SoC < 0.94 (**g**). a.u., atomic units. **h**, The Ni–O_1 bond length and Debye–Waller factor of EEC–Ni90 cathode as a function of SoC, collected from the fitting of corresponding EXAFS spectra with a sample size of 21. The error bar indicates the error range during EXAFS fitting.

the reported Ni-rich cathodes without coating[43,44]. The in situ BCDI of bare Ni90 cathode during charging was also conducted for comparison, which, however, undergoes much more severe structural changes at a much lower SoC (Supplementary Fig. 22). The in situ BCDI and CMCD results combined with in situ HEXRD results collectively confirmed that the EEC layer could suppress lattice dislocation/strain generation and hence improve the phase transition reversibility and stability at both the particle and electrode levels.

In situ X-ray absorption spectroscopy (XAS) studies of the EEC–Ni90 cathode were conducted to further monitor the dynamic local structure changes during charge/discharge. As shown in the X-ray absorption near edge structure (XANES) results (Fig. 5a and Supplementary Fig. 23), the Ni K edge gradually shifted to higher energy during charge and then completely shifted back to its original position at the end of the initial discharge, indicating good reversibility of Ni redox in the EEC–Ni90. The extended X-ray absorption fine structure (EXAFS) in R space (Fig. 5b and Supplementary Fig. 24) revealed that the Ni–O_1 and Ni–TM bond lengths were gradually shortened during charge due to the oxidation of Ni upon delithiation[45]. After discharging to 2.5 V, the bond lengths of Ni–O_1 and Ni–TM could return to their pristine states, confirming the excellent redox reversibility.

Furthermore, when the SoC was lower than 0.52, the Ni K edge exhibited a gradual and gentle shift to higher energy, but a quick energy shift was observed when the SoC exceeded 0.56 (Fig. 5c), which is in contrast to polycrystalline Ni-rich cathodes[45,46] but similar to cracking-free single-crystalline Ni-rich cathodes[47,48]. The results indicated that the EEC layer could effectively mitigate the buildup of

https://doi.org/10.1038/s41560-024-01465-2

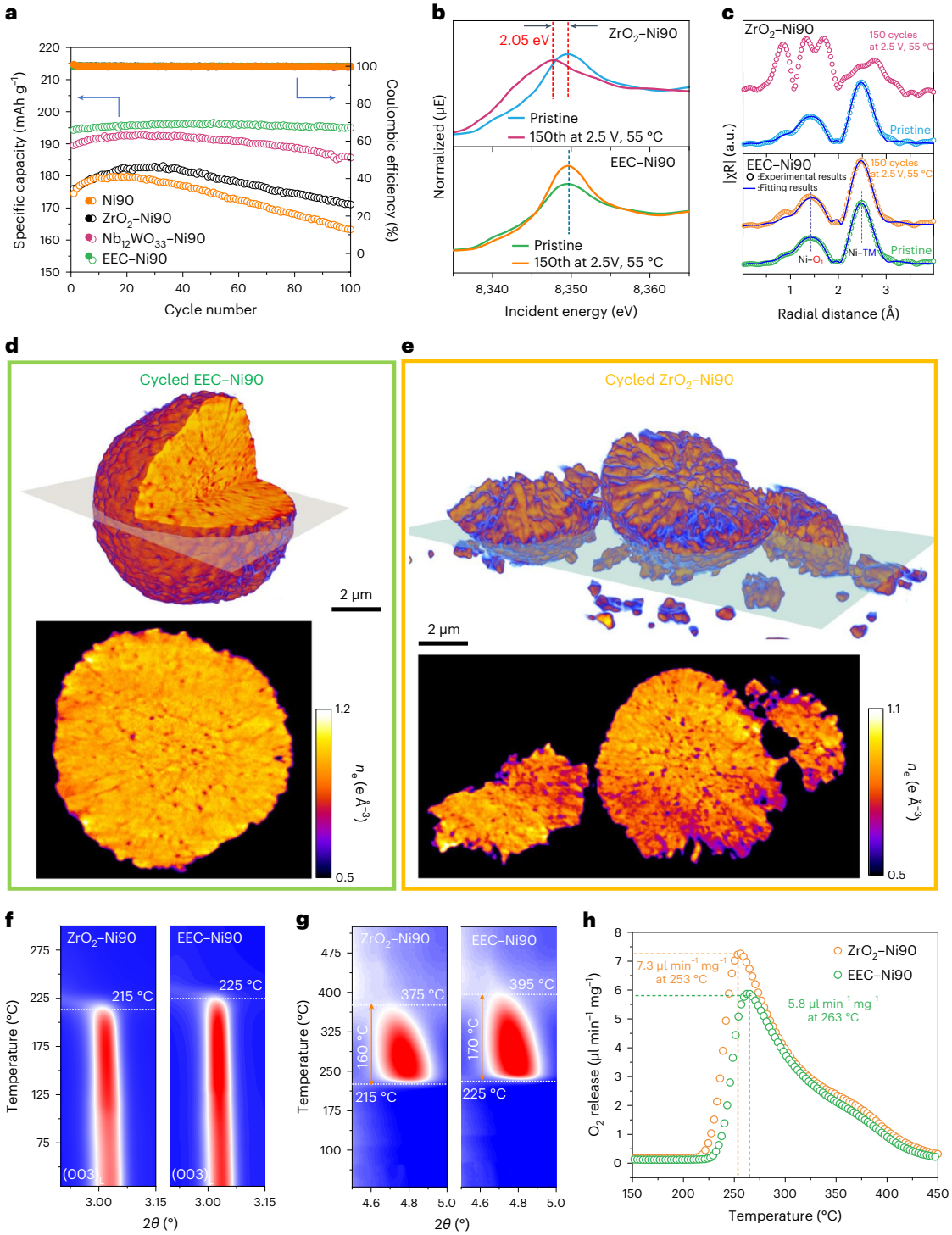

Fig. 6 | Comparison between entropy-assisted cathodes. a, Cycling performance of bare Ni90 and entropy-assisted coated Ni90 cathodes at 1C. Hollow and solid symbols represent the discharge capacity and Coulombic efficiency, respectively. **b**,**c**, XANES results (**b**) and EXAFS fitting results (**c**) of pristine and cycled EEC–Ni90 and ZrO$_2$–Ni90 cathodes after 150 cycles at 0.5C and 55 °C. **d**,**e**, Three-dimensional X-ray ptychography reconstruction of cycled EEC–Ni90 (**d**) and ZrO$_2$-Ni90 (**e**) cathode after 150 cycles at 0.5 C and 55 °C. **f**–**h**, In situ HEXRD patterns of 4.3 V-charged ZrO$_2$–Ni90 and EEC–Ni90 cathode –from 2θ 2.9–3.15° (**f**) and 2θ 4.5–5.0° (**g**) as well as the corresponding oxygen evolution (**h**) during heating. **f**,**g**, The dashed lines indicate the on-set temperature for phase transformation, and the arrows indicate the temperature range during the phase transformation. **h**, The dashed lines indicate the peak oxygen release rate and the corresponding temperature.

microstrain and prevent the mechanical breakdown of layered cathodes as single crystals. Moreover, the slow accumulation of Ni^{3+} and rapid oxidation of Ni^{3+} to Ni^{4+} during charging could suppress the structural instability and TM ion dissolution caused by the Jahn–Teller distortion active site (Ni^{3+}) (ref. 49). The zoom-in EXAFS spectra (Fig. 5e) also exhibited a slow shortening of Ni–O$_1$/Ni–TM bond lengths at low SoC, while further charging resulted in a sharp bond length decrease, which agreed well with the in situ XANES results. To quantify the dynamic

local structure changes and confirm our hypothesis, EXAFS fitting was conducted. The crystal structure model, scattering paths and fitting details can be found in Supplementary Figs. 25–27. It should be noted that the difference (~0.4 Å) between the measured and actual atomic distances is because of the phase shifts during the scattering process[50]. As shown in Fig. 5f,g and Supplementary Table 4, when the SoC was <0.52, the Ni–O_1 only exhibited 0.12% bond length shortening. Further charging to a high SoC of 0.94 led to a slight increase of Ni–O_1 bond length shortening to 3.31%. In addition, the Debye–Waller disorder factor of Ni–O (σ^2_{Ni-O}), which is directly associated with the Ni^{3+}-induced Jahn–Teller distortion, was also tracked for EEC–Ni90 during the initial cycle. No obvious increase of σ^2_{Ni-O} was observed for EEC–Ni90 during the charging process (Fig. 5h), which conflicts with previous in situ XAS studies for polycrystalline Ni-rich cathodes that exhibit a quick increase of the Debye–Waller disorder factor at the early delithiation stage owing to the rapid accumulation of Jahn–Teller active Ni^{3+}(refs. 45,51,52).

As a consequence, benefitting from the epitaxial entropy-assisted surface nature, the EEC layer could improve the structural stability of ultrahigh-Ni cathodes during long-term cycling, as evidenced by the high-angle annular dark-field scanning transmission electron microscopy (HAADF–STEM) characterization on the cycled EEC–Ni90 cathode (Supplementary Figs. 28, 29).

Comparison with conventional oxide coating

To further highlight the advantages of the epitaxial entropy-assisted coating, comparisons between EEC–Ni90 and conventional oxide coated Ni90 (ZrO_2–Ni90 and $Nb_{12}WO_{33}$–Ni90) were conducted. As shown in Fig. 6a, the cycling stability of Ni90 cathodes during charge/discharge at 1C is in an order of bare Ni90 < ZrO_2–Ni90 < $Nb_{12}WO_{33}$–Ni90 < EEC–Ni90, which is well consistent with the number of elements in the coating layers. The XAS characterization of cycled electrodes (Fig. 6b) showed that no obvious peak shift was observed in the case of cycled EEC–Ni90. By contrast, without EEC layer, for example, the cycled ZrO_2–Ni90 exhibited a 2.05 eV peak shift to lower energy, indicating the dramatic structure collapse and severe Ni reduction after cycling at elevated temperature of 55 °C. Detailed EXAFS and corresponding fitting results (Fig. 6c and Supplementary Fig. 30) further confirmed the improved structural stability of EEC–Ni90 as evidenced by the negligible peak shift and bond length change after cycling (Supplementary Table 5). However, the EXAFS spectrum of cycled ZrO_2–Ni90 dramatically changed, and it could not be fitted using the $R\bar{3}m$ crystal model, indicating a severe phase transformation after long-term cycling. To directly visualize the improved morphological integrity by the entropy-assisted coating, 3D X-ray ptychography of cycled EEC–Ni90 and ZrO_2–Ni90 were performed. As shown in Fig. 6d,e, after cycling at 55 °C and 0.5C for 150 cycles, EEC–Ni90 could still maintain its polycrystalline morphology well and no obvious cracks could be observed in the cross-section image. However, in the case of cycled ZrO_2–Ni90, the particles were severely cracked into isolated fragments.

The thermal stability of 4.3 V-charged EEC–Ni90 and ZrO_2–Ni90 cathodes was further evaluated through in situ HEXRD coupled with mass spectrometry during heating. As shown in Fig. 6f,g and Supplementary Fig. 31, both charged cathodes exhibited a typical rhombohedral ($R\bar{3}m$)–spinel ($Fd3m$)–rock salt ($Fm\bar{3}m$) phase transformation during heating[53], which are typically accompanied with severe transition metal migration/reduction and oxygen gas release, and hence strongly correlated with battery safety. Charged EEC–Ni90 exhibited higher onset temperature for layered-to-spinel (225 °C) and spinel-to-rock salt (395 °C) transformation than that of charged ZrO_2–Ni90 (215 °C and 375 °C, respectively). Moreover, the oxygen release rate was notably reduced by 20% with a higher maximum release temperature in the EEC–Ni90 cathode (Fig. 6h).

Differential scanning calorimetry (DSC) testing (Supplementary Fig. 32 and Table 6) of electrochemically delithiated (80% SoC) bare Ni90, ZrO_2–Ni90 and EEC–Ni90 cathode showed two distinct exothermic peaks, corresponding to the layered-to-spinel and spinel-to-rock salt phase transition, respectively. As shown, both two exothermic peaks, in particular the spinel-to-rock salt phase transition of the charged cathode, were postponed to higher temperature with dramatically reduced heat generation by epitaxial entropy-assisted coating. All these results confirm that the entropy-assisted surface design can better stall the labile oxygen loss and the associated structural degradation than a conventional low-entropy oxide coating strategy, resulting in better cycle life and safety.

Conclusions

A universal epitaxial entropy-assisted coating strategy with robust electro-chemomechanical resistance was developed to address the progressive strain propagation in ultrahigh-Ni NCM cathodes during fast charging and long-term cycling. We discovered that the unique ReO_3-type block in the Wadsley–Roth family of crystallographic shear structures can enable an oriented attachment-driven reaction with layered-oxide cathodes to form an entropy-assisted phase. Such an epitaxial entropy-assisted surface not only effectively enhances the structural stability of ultrahigh-Ni cathodes under extreme operating conditions but also facilitates the Li^+ transport to ensure fast (de) lithiation redox kinetics, avoiding the trade-off dilemma between cycle stability and energy/power density. As evidenced by a combination of synchrotron X-ray imaging, diffraction and absorption techniques, the lattice dislocation, anisotropic lattice parameter changes and microstrain buildup as well as the consequent mechanochemical breakdown are effectively mitigated, even during fast charging and long-term cycling. We expect that such an epitaxial entropy-assisted coating strategy will open up surface engineering opportunities for the design and development of high-energy and high-power lithium ion batteries and beyond.

Methods

Preparation of Ni90

The $Ni_{0.9}Co_{0.05}Mn_{0.05}(OH)_2$ precursor was prepared via a co-precipitation process. Afterwards, the precursor was mixed with $LiOH{\cdot}H_2O$ at a molar ratio of Li:(Ni + Co + Mn) 1.05:1 in a high-speed Resodyn Acoustic mixing machine. Then, the mixture was heated in a 750 °C tube furnace for 15 h under the O_2 atmosphere. The obtained powder was washed with an equal weight amount of water for 20 min to remove the excess residual compounds. After collecting the powder via filtration, the powder was then dried in a 150 °C vacuum oven for 10 h. Then, the obtained powder was calcined in a 400 °C tube furnace for 6 h under O_2 atmosphere to obtain the Ni90 cathode powder.

Preparation of nano-sized $Nb_{12}WO_{33}$

In a typical synthesis, 159.48 g Nb_2O_5 and 23.18 g WO_3 were mixed well. Then, the mixture was heated in a 1,100 °C muffle furnace for 8 h. The particle size of the product was then reduced through a sand-milling method with a solid content of 30% for 3 h. The obtained nano-sized $Nb_{12}WO_{33}$ powder was then dried via a spray-drying method. Afterwards, the nano-sized $Nb_{12}WO_{33}$ powder was mixed in a planetary ball mill to further disperse it.

Preparation of EEC–Ni90

The precursor powder was prepared by mixing Ni90 powder, nano-sized $Nb_{12}WO_{33}$ powder and nano-sized ZrO_2 powder based on a weight ratio of 1:0.001:0.004 in a high-speed Resodyn Acoustic mixing machine for 15 min. Then, the precursor powder was heated in a 700 °C tube furnace for 4 h under an O_2 atmosphere.

Preparation of ZrO_2–Ni90

The as-synthesized $Ni_{0.90}Co_{0.05}Mn_{0.05}(OH)_2$ precursor was mixed with $LiOH{\cdot}H_2O$ and ZrO_2 (99.99%, ≤100 nm, Aladdin) at a molar ratio of

Li:(Ni + Co + Mn):Zr of 1.05:0.996:0.004 in a high-speed Resodyn Acoustic mixing machine. The mixture was then heated in a 750 °C tube furnace for 15 h under O_2 atmosphere. The obtained powder was washed with equal weight amount of water for 20 min to remove the excess residual compounds. After collecting the powder via filtration, the powder was then dried in a 150 °C vacuum oven for 10 h. Then, the obtained powder was calcined in a 400 °C tube furnace for 6 h under O_2 atmosphere to get the ZrO_2–Ni90 cathode.

Preparation of $Nb_{12}WO_{33}$–Ni90

$Nb_{12}WO_{33}$–Ni90 was prepared by mixing Ni90 powder and nano-sized $Nb_{12}WO_{33}$ powder based on a weight ratio of 1:0.005 in a high-speed Resodyn Acoustic mixing machine for 15 min. Then, the mixture was annealed in a 700 °C tube furnace for 4 h under O_2 atmosphere.

Physical structure characterization

The SEM characterizations were conducted by using a JEOL JSM-7100F. The TEM characterizations were conducted by using an FEI F200X and JEOL 2100F. The cross-section samples were prepared via using a focused ion beam SEM dual-beam system (Zeiss Nvision 40). The powder X-ray diffraction characterizations of various NCM powders were carried out using the synchrotron XRD at Beamline 17-BM of the Advanced Photon Source (APS) at Argonne National Laboratory.

ToF–SIMS characterization of cycled Li metal anode

The cycled cells were disassembled in an Ar-filled glove box, and the cycled Li metal foils were carefully taken out and rinsed with fresh ethyl methyl carbonate solvent to remove the electrolyte. Afterwards, the dried Li metal anodes were mounted on an Ar-filled capsule and transferred into the IONTOF M6 testing chamber. A 500 eV 50 nA CS^+ ion beam was used for sputtering the sample with an analysed area of 50 μm × 50 μm.

Cross-section SEM of cycled cathode

The cycled cells were disassembled in an Ar-filled glove box, and the cycled cathodes were carefully taken out and rinsed with fresh ethyl methyl carbonate solvent to remove the electrolyte. Afterwards, the cross-section samples were prepared using Ar^+ ion beam at 4.0 kV for 6 h followed by 3.0 kV for 1 h to get smooth surface with a cross-section polisher, located in a dry room. The cross-section samples were transferred into the SEM chamber using the air-tight sample holder to minimize air and moisture exposure. The JEOL JSM-6610 LV SEM instrument was used for investigation.

In situ HEXRD during heating of precursors

The in situ HEXRD during heating of Ni90, nano-$Nb_{12}WO_{33}$ and nano-ZrO_2 with a weight ratio of 1:1:1 was conducted at Beamline 17-BM (λ = 0.24095 Å). The precursor powders were loaded in a quartz capillary tube connected with pure O_2 gas flow and put in controllable heating equipment. The samples were heated to 600 °C with a heating rate of 5 °C min^{-1} and then held at 600 °C for 5 h.

In situ HEXRD during charge/discharge

The in situ HEXRD of the EEC–Ni90 and Ni90 cathodes during charge/discharge were conducted at Beamline 17-BM (λ = 0.24079 Å) of the APS. The in situ cells were cycled within 2.5–4.3 V at 0.1C. A lanthanum hexaboride standard sample was used to calibrate the diffraction patterns, followed by the integration of diffraction peaks in the GSAS II software. Rietveld refinements of the in situ HEXRD diffraction patterns were performed using the GSAS II software to collect the lattice parameters.

In situ HEXRD of charged cathodes during heating

The in situ HEXRD during heating of charged EEC–Ni90 and charged ZrO_2–Ni90 cathodes was conducted at Beamline 17-BM (λ = 0.24079 Å). The EEC–Ni90 and ZrO_2–Ni90 cathodes were both charged to 4.3 V. Then, the as-collected cathode powder was loaded into a quartz capillary tube and put into a controllable heating setup. A residual gas analyser (RGA, QMG 220; PrismaPlus) was used to analyse the gas generation during heating. A lanthanum hexaboride standard sample was used to calibrate the diffraction patterns, followed by the integration of diffraction peaks in the GSAS II software.

In situ BCDI and CMCD during charge/discharge

The in situ CMCD during charge/discharge of the EEC–Ni90 cathode was carried out at Beamline 34-ID-C of the APS. The X-rays were selected by a double-crystal monochromator at 9 keV energy. The beam was focused by a pair of Kirkpatrick–Baez mirrors to a 1 mm × 1 mm spot size on the sample. A Princeton Instrument charge-coupled device (CCD) detector was located 270 mm downstream to measure the [300] reflection of the sample. The CCD had 1,300 × 1,340 pixels with a 22.5 mm × 22.5 mm pixel size. The diffraction signals of tens of primary particles were collected by the CCD repeatedly under coin-cell operando conditions. The coin cell was cycled at a 0.3C rate against a constant current with a Biologic SP300 potentiostat.

The in situ BCDI characterization was also conducted at Beamline 34-ID-C with 10 keV coherent X-rays and a spot size of ~600 nm on the sample. The 3D diffraction patterns of the [003] reflection from a primary particle were collected repeatedly during the initial charge process with a 0.1C cycling rate against a constant current. The instrumental and experimental details and data processing can be found in our previous work[40].

In situ and ex situ XAS studies

The XAS characterizations were conducted at Beamline 20-BM of the APS. The in situ coin cell was assembled using EEC–Ni90 as the cathode and lithium metal foil as the anode in a coin-type cell with two holes (ϕ = 2 mm) on both the cathode and anode cases. The in situ cells were charged/discharged between 2.5 and 4.3 V at 0.1 C using a MACCOR battery cycler. The XANES and EXAFS results were extracted and normalized by established methods using the ATHENA software package. The EXAFS data fitting was conducted within the radial distance range of 1.0–3.5 Å using the ARTEMIS software package.

X-ray ptychography

Three-dimensional X-ray ptychography of cycled EEC–Ni90 and ZrO_2–Ni90 cathodes was conducted on the Velociprobe[54] located at Beamline 2-ID-D of the APS. The EEC–Ni90 and ZrO_2–Ni90 cathodes were first charged/discharged in coin-type cells for 100 cycles under the rate of 0.5C within 2.5–4.3 V at 55 °C. Then, the cycled cathode powder was collected and dispersed on Si_3N_4 membrane (thickness of 200 nm). Details of experiment and data processing can be found from our previous publications[53].

Electrochemical characterization

The slurries consisted of active material, carbon black (C45 conductive carbon black, TIMCAL) and polyvinylidene fluoride (PVDF) with a weight ratio of 8:1:1, dispersed in a certain amount of *N*-methyl-2-pyrrolidone solvent. For the high areal loading cathode (~20 mg cm^{-2}), the weight ratio of active material, PVDF and carbon black was 92:4:4. After fine grinding in a motor at 2,000 rpm for 10 min, the as-collected slurry was cast on the surface of Al foil and dried at 80 °C under vacuum overnight. For the coin-type cell, the cathode was punched into round electrodes with a diameter of 14 mm, and the 2,032-type coin-cell case was used for coin-cell assembly. Upon coin-cell assembly, the lithium metal foil (diameter, ϕ = 16 mm; thickness, d = 0.6 mm) was used as the anode, Celgard 2325 was used as the separator and the Gen II (1.2 M $LiPF_6$ in ethylene carbonate/ethyl methyl carbonate, v/v of 3/7) with 2 wt% VC additive was used as the electrolyte unless otherwise specified. The areal loading of the cathode was ~6.0 mg cm^{-2} unless specially noted in the corresponding figures. For the pouch-type cell, the as-prepared

cathode was cut into 5 cm × 8 cm pieces, and another piece of Cu foil with the same size was used as the anode current collector. A piece of 5 cm × 8 cm Li metal foil was rolling-pressed on the surface of a Cu foil as the anode. Celgard 2325 was used as the separator, and Gen II was used as the electrolyte. Unless specified, all the cells were tested within 2.5–4.3 V using LanDdt CT2001 or MACCOR battery cycler. The cells used for GITT tests were first formation at 0.1C for three cycles. Then, the GITT measurements were further conducted with the titration step at 0.1C for 20 min and a relaxation step of 1 h.

DSC investigations of electrochemically delithiated cathodes

All testing cathodes were electrochemically delithiated with the same capacity of 220 mAh g^{-1} at 0.1C. The charged cells were opened in an Ar-filled glove box. The charged electrodes were then rinsed with 2 ml ethyl methyl carbonate twice and vacuum dried before the thermal stability experiment using a DSC 6000 (Perkin Elmer). Typically, a DSC sample includes about 3 mg of powder material from the harvested electrode. The sample was loaded into a stainless steel DSC cell and then sealed. The test was carried out between 50 °C to 385 °C with a scan rate of 5 °C min^{-1}. The heat flow detected was then calculated according to the weight of the cathode powder.

Data availability

The data supporting the findings of this study are included within the article and its Supplementary Information files. Source data are provided with this paper.

References

1. Li, W., Erickson, E. M. & Manthiram, A. High-nickel layered oxide cathodes for lithium-based automotive batteries. *Nat. Energy* **5**, 26–34 (2020).
2. Liu, J. et al. Pathways for practical high-energy long-cycling lithium metal batteries. *Nat. Energy* **4**, 180–186 (2019).
3. Xu, C. et al. Bulk fatigue induced by surface reconstruction in layered Ni-rich cathodes for Li-ion batteries. *Nat. Mater.* **20**, 84–92 (2021).
4. Lin, F. et al. Surface reconstruction and chemical evolution of stoichiometric layered cathode materials for lithium-ion batteries. *Nat. Commun.* **5**, 3529 (2014).
5. Cai, M. et al. Stalling oxygen evolution in high-voltage cathodes by lanthurization. *Nat. Energy* **8**, 159–168 (2023).
6. Lin, F., Zhao, K. & Liu, Y. Heterogeneous reaction activities and statistical characteristics of particle cracking in battery electrodes. *ACS Energy Lett.* **6**, 4065–4070 (2021).
7. Li, J. et al. Dynamics of particle network in composite battery cathodes. *Science* **376**, 517–521 (2022).
8. Li, W., Asl, H. Y., Xie, Q. & Manthiram, A. Collapse of $LiNi_{1-x-y}Co_xMn_yO_2$ lattice at deep charge irrespective of nickel content in lithium-ion batteries. *J. Am. Chem. Soc.* **141**, 5097–5101 (2019).
9. Yan, P. et al. Coupling of electrochemically triggered thermal and mechanical effects to aggravate failure in a layered cathode. *Nat. Commun.* **9**, 2437 (2018).
10. Yan, P. et al. Intragranular cracking as a critical barrier for high-voltage usage of layer-structured cathode for lithium-ion batteries. *Nat. Commun.* **8**, 14101 (2017).
11. Zhan, C., Wu, T., Lu, J. & Amine, K. Dissolution, migration, and deposition of transition metal ions in Li-ion batteries exemplified by Mn-based cathodes—a critical review. *Energy Environ. Sci.* **11**, 243–257 (2018).
12. Xiang, Y. et al. Gas induced formation of inactive Li in rechargeable lithium metal batteries. *Nat. Commun.* **14**, 177 (2023).
13. Xia, S. et al. Chemomechanical interplay of layered cathode materials undergoing fast charging in lithium batteries. *Nano Energy* **53**, 753–762 (2018).
14. Hu, E., Wang, X., Yu, X. & Yang, X.-Q. Probing the complexities of structural changes in layered oxide cathode materials for Li-ion batteries during fast charge–discharge cycling and heating. *Acc. Chem. Res.* **51**, 290–298 (2018).
15. Tanim, T. R. et al. Extended cycle life implications of fast charging for lithium-ion battery cathode. *Energy Storage Mater.* **41**, 656–666 (2021).
16. Li, J. et al. Multiphase, multiscale chemomechanics at extreme low temperatures: battery electrodes for operation in a wide temperature range. *Adv. Energy Mater.* **11**, 2102122 (2021).
17. Chen, Z., Qin, Y., Amine, K. & Sun, Y. K. Role of surface coating on cathode materials for lithium-ion batteries. *J. Mater. Chem.* **20**, 7606–7612 (2010).
18. Gao, H. et al. Modifying the surface of a high-voltage lithium-ion cathode. *ACS Appl. Energy Mater.* **1**, 2254–2260 (2018).
19. Yan, P. et al. Tailoring grain boundary structures and chemistry of Ni-rich layered cathodes for enhanced cycle stability of lithium-ion batteries. *Nat. Energy* **3**, 600–605 (2018).
20. Xu, G.-L. et al. Building ultraconformal protective layers on both secondary and primary particles of layered lithium transition metal oxide cathodes. *Nat. Energy* **4**, 484–494 (2019).
21. Nisar, U., Muralidharan, N., Essehli, R., Amin, R. & Belharouak, I. Valuation of surface coatings in high-energy density lithium-ion battery cathode materials. *Energy Storage Mater.* **38**, 309–328 (2021).
22. Ren, J. et al. Strong yet ductile nanolamellar high-entropy alloys by additive manufacturing. *Nature* **608**, 62–68 (2022).
23. Zeng, Y. et al. High-entropy mechanism to boost ionic conductivity. *Science* **378**, 1320–1324 (2022).
24. Yang, B. et al. High-entropy enhanced capacitive energy storage. *Nat. Mater.* **21**, 1074–1080 (2022).
25. Ma, Y. et al. High-entropy energy materials: challenges and new opportunities. *Energy Environ. Sci.* **14**, 2883–2905 (2021).
26. Zhang, R. et al. Compositionally complex doping for zero-strain zero-cobalt layered cathodes. *Nature* **610**, 67–73 (2022).
27. Tan, X. et al. High-entropy surface complex stabilized $LiCoO_2$ cathode. *Adv. Energy Mater*. https://doi.org/10.1002/aenm.202300147 (2023).
28. Zhao, C., Ding, F., Lu, Y., Chen, L. & Hu, Y.-S. High-entropy layered oxide cathodes for sodium-ion batteries. *Angew. Chem. Int. Ed.* **59**, 264–269 (2020).
29. Fu, F. et al. Entropy and crystal-facet modulation of P2-type layered cathodes for long-lasting sodium-based batteries. *Nat. Commun.* **13**, 282 (2022).
30. Penn, R. L. & Banfield, J. F. Imperfect oriented attachment: dislocation generation in defect-free nanocrystals. *Science* **281**, 969–971 (1998).
31. Liu, Y. et al. Oriented attachment revisited: does a chemical reaction occur? *Matter* **1**, 690–704 (2019).
32. Griffith, K. J., Wiaderek, K. M., Cibin, G., Marbella, L. E. & Grey, C. P. Niobium tungsten oxides for high-rate lithium-ion energy storage. *Nature* **559**, 556–563 (2018).
33. MacArthur, K. E. et al. Optimizing experimental conditions for accurate quantitative energy-dispersive x-ray analysis of interfaces at the atomic scale. *Microsc. Microanal.* **27**, 528–542 (2021).
34. Lu, P., Moya, J. M., Yuan, R. & Zuo, J. M. Studies of X-ray localization and thickness dependence in atomic-scale elemental mapping by STEM energy-dispersive X-ray spectroscopy using single-frame scanning method. *Ultramicroscopy* **186**, 23–29 (2018).
35. Yuan, K. et al. Self-ball milling strategy to construct high-entropy oxide coated $LiNi_{0.8}Co_{0.1}Mn_{0.1}O_2$ with enhanced electrochemical performance. *J. Adv. Ceram.* **11**, 882–892 (2022).
36. Mao, Y. et al. High-voltage charging-induced strain, heterogeneity, and microcracks in secondary particles of a nickel-rich layered cathode material. *Adv. Funct. Mater.* **29**, 1900247 (2019).

37. Liu, T. et al. Rational design of mechanically robust Ni-rich cathode materials via concentration gradient strategy. *Nat. Commun.* **12**, 6024 (2021).
38. Xu, C., Reeves, P. J., Jacquet, Q. & Grey, C. P. Phase behavior during electrochemical cycling of Ni-rich cathode materials for Li-ion batteries. *Adv. Energy Mater.* **11**, 2003404 (2021).
39. Wang, L. G., Liu, T. C., Wu, T. P. & Lu, J. Strain-retardant coherent perovskite phase stabilized Ni-rich cathode. *Nature* **611**, 61–67 (2022).
40. Li, L. X., Xie, Y. Y., Maxey, E. & Harder, R. Methods for operando coherent X-ray diffraction of battery materials at the advanced photon source. *J. Synchrotron Radiat.* **26**, 220–229 (2019).
41. Ulvestad, A. et al. Topological defect dynamics in operando battery nanoparticles. *Science* **348**, 1344–1347 (2015).
42. Singer, A. et al. Nucleation of dislocations and their dynamics in layered oxide cathode materials during battery charging. *Nat. Energy* **3**, 641–647 (2018).
43. Liu, T. et al. Origin of structural degradation in Li-rich layered oxide cathode. *Nature* **606**, 305–312 (2022).
44. Estandarte, A. K. C. et al. Operando bragg coherent diffraction imaging of $LiNi_{0.8}Mn_{0.1}Co_{0.1}O_2$ primary particles within commercially printed NMC811 electrode sheets. *ACS Nano* **15**, 1321–1330 (2021).
45. Tallman, K. R. et al. Nickel-rich nickel manganese cobalt (NMC622) cathode lithiation mechanism and extended cycling effects using operando X-ray absorption spectroscopy. *J. Phys. Chem. C* **125**, 58–73 (2021).
46. Tsai, Y. W., Lee, J. F., Liu, D. G. & Hwang, B. J. In situ X-ray absorption spectroscopy investigations of a layered $LiNi_{0.65}Co_{0.25}Mn_{0.1}O_2$ cathode material for rechargeable lithium batteries. *J. Mater. Chem.* **14**, 958–965 (2004).
47. Ma, L., Wang, L., Liu, T., Wu, T. & Lu, J. Probing distinctive redox mechanism in Ni-rich cathode via real-time quick X-ray absorption spectroscopy. *Small Methods* **7**, 2201173 (2023).
48. Bi, Y. et al. Reversible planar gliding and microcracking in a single-crystalline Ni-rich cathode. *Science* **370**, 1313–1317 (2020).
49. Asl, H. Y. & Manthiram, A. Reining in dissolved transition metal ions. *Science* **369**, 140–141 (2020).
50. Rehr, J. J. & Albers, R. C. Theoretical approaches to X-ray absorption fine structure. *Rev. Mod. Phys.* **72**, 621–654 (2000).
51. Yoon, W.-S. et al. Investigation of the charge compensation mechanism on the electrochemically Li-ion deintercalated $Li_{1-x}Co_{1/3}Ni_{1/3}Mn_{1/3}O_2$ electrode system by combination of soft and hard X-ray absorption spectroscopy. *J. Am. Chem. Soc.* **127**, 17479–17487 (2005).
52. Yoon, W.-S., Grey, C. P., Balasubramanian, M., Yang, X.-Q. & McBreen, J. In situ X-ray absorption spectroscopic study on $LiNi_{0.5}Mn_{0.5}O_2$ cathode material during electrochemical cycling. *Chem. Mater.* **15**, 3161–3169 (2003).
53. Liu, X. et al. Origin and regulation of oxygen redox instability in high-voltage battery cathodes. *Nat. Energy* **7**, 808–817 (2022).
54. Deng, J. et al. The Velociprobe: an ultrafast hard X-ray nanoprobe for high-resolution ptychographic imaging. *Rev. Sci. Instrum.* **90**, 083701 (2019).

Acknowledgements

Research at the Argonne National Laboratory was funded by the US Department of Energy, Vehicle Technologies Office. Use of the APS and the Center for Nanoscale Materials, both Office of Science user facilities, was supported by the US Department of Energy, Office of Science and Office of Basic Energy Sciences, under contract no. DE-AC02-06CH11357. G.-L.X. and K.A. thank the Clean Vehicle Consortium, US–China Clean Energy Research Center (CERC-CVC2), for support.

Author contributions

G.-L.X., C.Z. and K.A. conceived the ideas. G.-L.X. and K.A. supervised the project. C.W., C.Z., J.-T. L. and S.-G.S. developed and synthesized cathode materials. C.Z. conducted electrochemical tests for various cells. Y.L., C.Z., G.W. and X.Z. conducted the TEM and SEM characterizations. Z.Y. conducted the cross-section SEM characterizations. C.Z., X.L., T.L. and W.X. carried out synchrotron HEXRD studies of various materials. L.L. and C.Z. conducted the in situ CMCD and BCDI characterization and analysis with the help of J. Diao, L.W., W.C., R.H. and I.R. I.H., C.S. and C.Z. conducted the XAS studies of various materials. J. Deng conducted the X-ray ptychography and data processing with the help of Y.J. and T.B. Y.Q. and W.L. conducted DSC tests. G.-L.X. and C.Z. drafted the paper with the help of all the other authors.

Competing interests

For G.-L.X., C.Z., Y.L. and K.A., a US non-provisional patent application, patent application no. 17/955,092, has been filed for this work. The patent is related to the coating strategy reported in this work and submitted by Argonne National Laboratory. All other authors declare no competing interests.

Additional information

Supplementary information The online version contains supplementary material available at https://doi.org/10.1038/s41560-024-01465-2.

Correspondence and requests for materials should be addressed to Luxi Li, Yuzi Liu, Gui-Liang Xu or Khalil Amine.

Peer review information *Nature Energy* thanks Ben Breitung and the other, anonymous, reviewer(s) for their contribution to the peer review of this work.